Exploring the Atwood-number dependence of the highly nonlinear Rayleigh-Taylor instability regime in high-energy-density conditions

G. Rigon [1,2,*] B. Albertazzi,[1] P. Mabey,[1,3] Th. Michel [1] E. Falize,[4] V. Bouffetier,[5]
L. Ceurvorst,[5] L. Masse,[4] M. Koenig,[1,6] and A. Casner [5,7]

[1]*LULI, CNRS, CEA, Ecole Polytechnique, UPMC, Univ Paris 06, Sorbonne Universités, Institut Polytechnique de Paris,
F-91128 Palaiseau cedex, France*

[2]*JSPS International Research Fellow, Graduate School of Science, Nagoya University, Furo-cho, Chikusa-ku, Nagoya 464-8602, Japan*

[3]*Freie Universität Berlin, Department of Physics, Arnimallee 14, 14195 Berlin, Germany*

[4]*CEA-DAM, DIF, F-91297 Arpajon, France*

[5]*Université de Bordeaux-CNRS-CEA, CELIA, UMR 5107, F-33405 Talence, France*

[6]*Graduate School of Engineering, Osaka University, Osaka, 565-0871, Japan*

[7]*CEA-CESTA, 15 avenue des Sablires, CS 60001, 33116 Le Barp Cedex, France*

We experimentally study the late-time, highly nonlinear regime of the Rayleigh-Taylor instability in a decelerating phase. A series of laser-driven experiments is performed on the LULI2000 laser, in which the initial Atwood number is varied by adjusting the decelerating medium density. The high-power laser is used in a direct drive configuration to put into motion a solid target. Its rear side, which initially possesses a two-dimensional machined sinusoidal perturbations, expands and decelerates into a foam leading to a Rayleigh-Taylor unstable situation. The interface position and morphology are measured by time-resolved x-ray radiography. We develop a simple Atwood-dependent model describing the motion of the decelerating interface, from which its acceleration history is obtained. The measured amplitude of the instability, or mixing zone width, is then compared with late-time acceleration-dependent Rayleigh-Taylor instability models. The shortcomings of this classical model, when applied to high-energy-density conditions, are shown. This calls into question their uses for systems, where a shock wave is present, such as those found in laboratory astrophysics or in inertial confinement fusion.

I. INTRODUCTION

Rayleigh-Taylor instability (RTI) [1,2] is a seminal hydrodynamic instability, ubiquitous in the universe, which pervades at all scales from Bose-Einstein condensates [3] to astrophysical distances [4,5]. This instability leads to the growth of the perturbation at the interface between fluids as soon as the scalar product between pressure and density gradients is negative. On Earth, this necessary condition is reached when a denser fluid rests on top of one of lower density, or in the case of interface acceleration. RTI has therefore a great impact on fluid dynamics in numerous systems [6–11].

Despite its apparent simplicity, RTI remains nowadays an active field of study as testified by the recent reviews [12–14]. This is partially due to the complexity of all nonlinear systems in fluid dynamics. Indeed, strikingly, even the late-time growth of single-mode RTI is not well understood [15]. After the linear phase of growth, the instability pattern becomes asymmetric [16]. The heavy fluid falls as spikes into the lighter fluid, and the lighter fluid rises as bubbles into the heavy fluid due to buoyancy forces. A key parameter is the initial Atwood number $A_t = (\rho_1 - \rho_2)/(\rho_1 + \rho_2)$, ρ_i being the i-fluid density. Based on the potential flow theory of Layzer [17], a terminal bubble velocity was proposed by Goncharov

for any Atwood number [18]. However, this theory breaks down for a 3D single mode as numerically evidenced for various Atwood numbers [19,20]. A reacceleration stage is predicted to occur for the bubble velocity when the secondary Kelvin-Helmholtz instabilities develop along the RTI spikes. Vorticity accumulates inside the RTI bubble inducing its reacceleration [21]. A similar phenomenon was demonstrated at the ablation front in the context of inertial confinement fusion (ICF) [22]. RTI in the acceleration [10,11] or deceleration phase [23–25] remains a major challenge towards a burning plasma in ICF. From an experimental point of view, while RTI has been widely studied in shock tube experiments [26], a parametric scan in Atwood numbers requires different gas mixtures [27,28]. Furthermore, a precise control and knowledge of the initial conditions remains challenging for any RTI experiments [29,30]. High-energy density (HED) settings allow one to circumvent these intrinsic limitations [31,32].

In this article, we explore the Atwood-number dependency of the RTI in HED conditions. This study builds upon the classical scheme of a laser-produced plasma expanding into a foam [33–36] with different densities. This HED platform is much simpler than traditional shock tube RTI platforms. Due to this simplicity, data sets are obtained, and a parametric study exploring different initial conditions is performed. Accurate measurements of acceleration and mixing zone widths are made and compared to classical models, which failed to reproduce the measurements. Explanations are suggested to
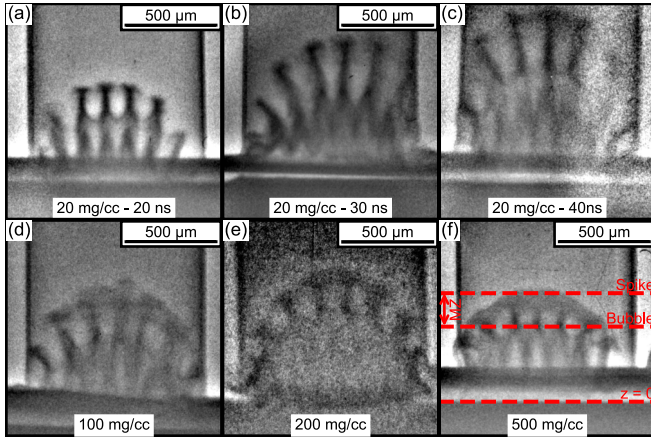
*gabriel.rigon@polytechnique.edu

FIG. 1. Example of obtained radiographies. The experimental radiographies (a, b, c) show the dynamic of the evolution of a 20 mg cm^{-3} foam. Similarly panels (d), (e), and (f) correspond to radiographs of 100, 200, and 500 mg cm^{-3} foams taken 30 ns after the laser shot. The initial wavelength λ is 120 μm.

understand the higher than expected RTI growths, a trend already observed in previous HED RTI settings [37,38].

II. EXPERIMENTAL SETUP

The experiments were performed on the LULI2000 laser facility using the setup described in [35]. The nano2000 laser beam (500 J, 2ω, 1.5 ns with a 470 μm super-Gaussian focal spot) deposits its energy on a multilayer target, with an intensity of 2×10^{14} W cm^{-2}. The target is composed of a 10 μm parylene ablator, a 1 μm gold x-ray shielding layer, and a 40 μm modulated pusher (C$_8$H$_7$Br). We employed three kind of modulations: a sine curve ($\lambda = 120$ μm wavelength, 10 μm amplitude), the sum of two sine curves [(70 and 130) μm wavelengths, (10 and 10) μm amplitudes], and flat targets. Here we will focus on single-mode data, as no obvious difference was observed between mono- and bimode [35]. As a consequence of the target ablation by the laser, a shock wave is launched into the target and put it into motion. The pusher expands into an external medium, a resorcinol formaldehyde (C$_{15}$H$_{12}$O$_4$) foam. Four foam densities were used: (20, 100, 200, and 500) mg cm^{-3}, leading to an initial Atwood number of 0.97, 0.87, 0.75, and 0.47, respectively. Since the ablation pressure applied by the laser is maintained only for $\sim$1.5 ns and since the foam has a non-negligible density, the expanding pusher decelerates resulting in a RT unstable situation.

To diagnose the interface between pusher and foam x-ray radiographs were taken (see Fig. 1). Those radiographs were performed by point projection [39], with an x-ray source produced by the pico2000 laser (55 J, 10 ps) focused on a 25 μm titanium wire (Kα x-ray emission line: $\sim$4.5 keV) and an imaging plate detector. This diagnostic presents a static $\lesssim$ 25 μm resolution [35]. It allows us to distinguish between pusher and foam, the contrast between the two being enhanced by the difference in density as well as the bromine doping of the pusher ($\sim$40% in mass). From those radiographs, two parameters are measured: the position of the central RTI spike and position of the central bubble extremities [cf. Fig. 1(f)].

We call the distance between spike and bubble extremities the mixing zone (MZ) width. In the case of the flat targets, the only observed variable is the actual interface position, which is needed to determine the RTI growth. To obtain the overall dynamics, we combine different single-snapshot radiographs acquired from similar targets, laser drive, and initial conditions [see Figs. 1(a)–(c)]. To compensate the laser energy fluctuations, we normalized the time delays with respect to the laser energy as explained in [35,40]: $\tilde{t} = t(E/E_0)^{1/3}$. Here we take 500 J as the reference laser drive energy (E_0).

To build more confidence in the experiments, we have conducted a series of radiation-hydrodynamics simulations using FLASH (v.4.5) [41,42]. We used it in a 2D Cartesian geometry in a hydrodynamic setup with three temperatures and an adaptive mesh refinement (paramesh4dev). We employed an "hllc" Riemann solver, an "mc" slope limiter, with a second-order data reconstruction (type MUSCL-Hancock) and a cfl of 0.3 in an unsplit solver scheme. The simulation domain we employed is a square with a length which varies between (800 and 1400) μm depending on the simulated case (far-reaching or not). It is divided in four main blocks, each subject to adaptive mesh refinement (AMR) up to the sixth order, and further divided in 16 cells in each spatial direction. This leads to a maximal resolution varying between (0.8 and 1.4) μm depending on the domain size. The AMR is based on the variation of density, temperature (electronic and ionic), and pressure. The laser intensity ($\simeq 5 \times 10^{13}$ W cm^{-2}) was adjusted to reproduce the initial experimental velocity for the interface between pusher and foam. And the laser pulse was modeled using 50 temporally equidistant points spanning from 0 to 2 ns. All the simulated plastic layers use the same IONMIX [43] tabulated equation of state (polystyrene) as well as their respective tabulated opacity calculated with PROPACEOS [44] with 40 radiation groups. The different elements of the experiment except the gold layer, which is too thin, are initialized in accordance with the geometry of the experiment (vacuum, ablator, pusher, foam, and tube).

In addition to these simulations, 1D simulations in Cartesian geometry were performed for the need of the alteration of the buoyancy-drag model discussed later. These simulations employed the same parameters as the 2D simulations except for the initial geometry and the laser intensity, which need to be lowered to obtain the right initial velocity.

III. INTERFACE MOTION

A. Measure of the position

We focus first on the motion of the interface between pusher and foam. Here by interface, we mean the position where the interface would be in the absence of RTI effects. Indeed, this motion triggers the consequent RTI growth. Since the interface is warped, due to the development of hydrodynamic instabilities, we theoretically cannot follow its motion except for the flat targets. As shown in Fig. 2(a), the movement of the interface is equal to the movement of the central RTI spike of the modulated targets. The difference in position is too small to distinguish between the two with our experimental resolution. This is also observed in simulations. In Fig. 2(b) the length of the spikes and bubbles is displayed.
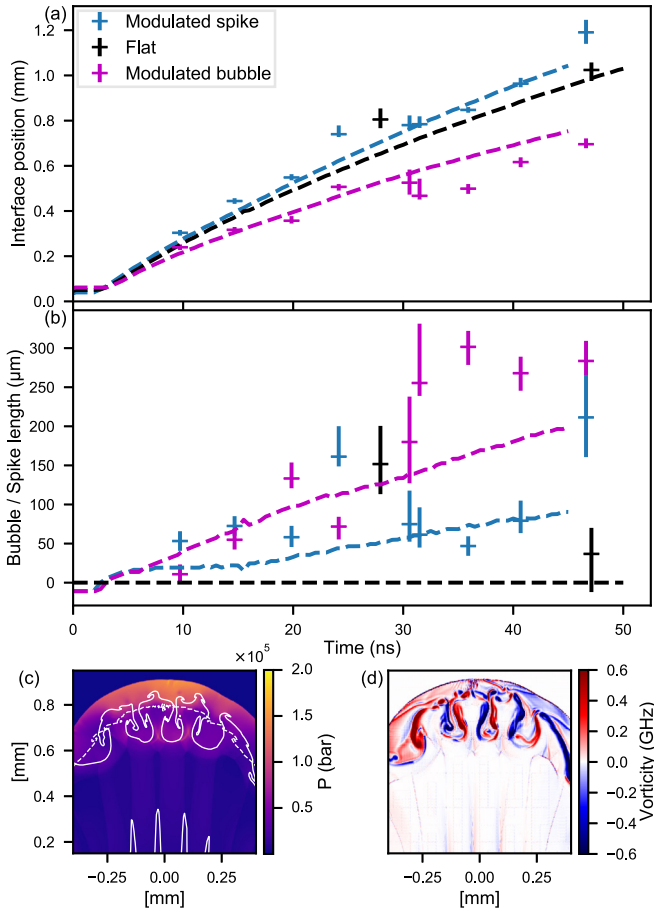
FIG. 2. Comparison between RTI spike and interface position. (a) Temporal evolution of the position of the spike (blue), bubble (magenta), and interface of a flat target (black) both experimentally (points data) and in simulation for a $20\,\mathrm{mg\,cm^{-3}}$ foam. (b) Temporal evolution of the bubble and spike lengths, which are calculated using the simulated interface position from (a). (c) Simulated pressure map taken 25 ns after shock break out around the interface. The interface between pusher and foam is depicted with a white full line for the modulated case and a dashed line for a flat target. (d) Map of the simulated vorticity in the z direction (curl of velocity projected on z axis) in the modulated case.

Here this length is calculated as the difference between their respective position and the position of the interface obtained through simulation ($x_{\mathrm{spike}} - x_{\mathrm{interface}}$ and $x_{\mathrm{interface}} - x_{\mathrm{bubble}}$). As can be seen, the spike length is lower than $100\,\mu\mathrm{m}$ (except for two out-of-curve experimental points) and has a minimal error of $25\,\mu\mathrm{m}$, which is the ideal static case. Thus, the experimental position of the spike and of the interface can be hardly distinguished experimentally. This is especially the case considering the experimental "length of the interface" (black dots), which should be equal to zero but is of the order of the length of the spikes. This is mainly due to a defect in the spike growth resulting from the proximity of the shock wave [45]. This fact is obvious in simulation as shown in Fig. 2(c), where the pressure and the interface morphology are displayed. The RTI spikes are subject to an excessive pressure, which reduces their growth. Thus, the position of the spikes corresponds approximately to the interface one. As
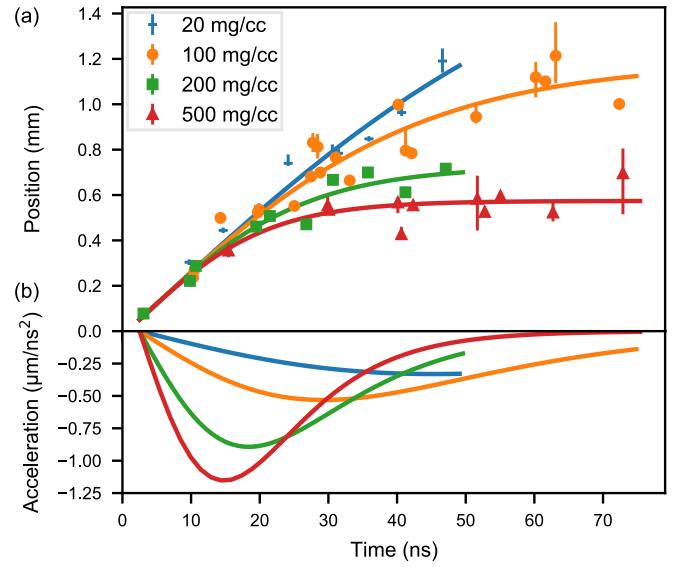

FIG. 3. Temporal dynamics of the interface. (a) Evolution of the interface position for the different foam densities (20, 100, 200, and 500) $\mathrm{mg\,cm^{-3}}$ corresponding to $A_t = 0.97, 0.87, 0.75,$ and 0.47. The scattered data points correspond to the obtained experimental results. The associated curves correspond to the result of our model (1) with an initial velocity fixed to $28\,\mu\mathrm{m\,ns^{-1}}$. (b) Acceleration of the interface deduced from the model [$\ddot{x}(t)$].

for the bubbles, they are easily distinguished from the spikes and interface.

The experimental data displayed in Fig. 3(a) thus correspond to the interface dynamics for each foam density. Each dynamics can be divided in two phases: ballistic and decelerating. The first phase corresponds to a nearly constant interface velocity. If we compare our experiment to the classical model of supernova remnant (SNR) expansion [46,47], this phase would correspond to the free expansion where the mass of swept external medium is still too small to influence the shock and interface dynamics. Here the interface velocity does not depend on the foam density, but on the ablator composition and on the momentum transmitted by the laser, both parameters kept constant. Following the SNR analogy, this ballistic phase ends as soon as a sufficient mass of foam is swept by the shock, which obviously happens sooner with higher foam density. In the following phase, the interface decelerates triggering the RTI growth. As expected, the deceleration increases with higher foam density. This is especially obvious with the two extreme cases [(20 and 500) $\mathrm{mg\,cm^{-3}}$]: for the low-density case, the motion remains ballistic, whereas it becomes quasistationary for the high one. Varying the initial foam density induces two opposing effects expected from the linear approximation of the RTI growth: a high density leads to a high deceleration, thus a high growth rate ($\propto \sqrt{g}$), and a low Atwood number, thus a low growth rate ($\propto \sqrt{A_t}$).

B. Analytical model

Before studying in detail the RTI growth, we develop an analytical approach of the interface motion. The following 1D analysis is based on two hypotheses: (1) the initial velocity of

the interface, v_0, is the same for every foam density and (2) the deceleration of the interface depends on the swept mass of foam and on the interface velocity. The first assumption is a given since the initial velocity of the interface depends on the momentum transmitted by the shock wave, which is the same for every target (same target composition and laser intensity). The dependence of the acceleration on the swept mass is not a far stretch in one dimension. Indeed, the shocked foam accumulates at the pusher front leading to an increased mass thus inertia. If we suppose the deceleration being proportional to the swept mass, then it will be proportional to the shock (or interface) position ($\ddot{x} \propto m_{swept} \propto x\rho_0$). Finally, the dependence of the deceleration on the interface velocity can be understood when considering that in a time step the pusher has to sweep a foam quantity proportional to its velocity ($\ddot{x} \propto \dot{x}$). Therefore, the interface dynamics should follow the differential equation: $\ddot{x} = -Bx\dot{x}$, with $B \propto \rho_0$ a constant. This equation admits for solution

$$x(t) = \sqrt{\frac{2v_0}{B}} \tanh \sqrt{\frac{Bv_0}{2}} t. \qquad (1)$$

Here $t = 0$ corresponds to the shock break out (2.5 ns) and $x = 0$ to the position of the interface at that time (50 μm). This coordinate system is a space-time translation of the experimental coordinates. It is used only in the following paragraph. We can fit this solution to our experimental results as shown in Fig. 3(a). If all fitting parameters are unconstrained, then the initial velocity, $v_0 = \dot{x}(t = 0)$, varies between (25.9 and 29.3) μm ns^{-1} depending on the data set. Since this variation is small and since all the initial velocities should be the same, we impose a v_0 of 28 μm ns^{-1}, which corresponds to our simulated data. B is then equal to (1.7 ± 0.2, 4.3 ± 0.1, 12.2 ± 0.4, and 20.3 ± 1.1) $\times 10^{-5}$ μm ns^{-1} for foam density of (20, 100, 200, and 500) mg cm^{-3} respectively. As predicted we find that B is nearly proportional to the foam density [$B/\rho_0 = (4.3 \pm 1.0) \times 10^5$ μm^2 mg^{-1} ns^{-1}]. The observed variation might be linked to some inaccuracy on the foam density or on our experiments process. Given our model, we can calculate the acceleration of the interface as a function of time [see Fig. 3(b)]. The temporal position of the maximum of each deceleration can be calculated [$\log(2 + \sqrt{3})/\sqrt{2Bv_0}$], thus determining the transition between the two phases (ballistic and decelerating). Here the maximal deceleration is attained at (43, 27, 16, and 12) ns after shot break-through (2.5 ns) for each respective density. The model was also tested on experimental results obtained on SACLA (Japanese XFEL) for the same kind of target (100 mg cm^{-3}) but with a lower laser intensity, $\sim 10^{13}$ W cm^2 [36]. Despite the lower initial interface velocity $v_0 = 10.5 \pm 0.2$ μm ns^{-1}, the model fit the data with the same B parameter as in LULI2000.

We should mention that the deceleration exists from the beginning of the interface motion according to our model [see Fig. 2(c)]. In that sense, the first phase of the evolution would be closer to the ejecta dominated self-similar (we do not know if there is self-similarity in our experiment) phase of the SNR dynamic [48,49]. To complete this parallel, we should add that the subsequent Sedov-Taylor phase should start when the mass of swept-up foam equal the expanding pusher mass. Assuming that our problem is monodimensional (no lateral expansion) and that the whole depth of the pusher is put in
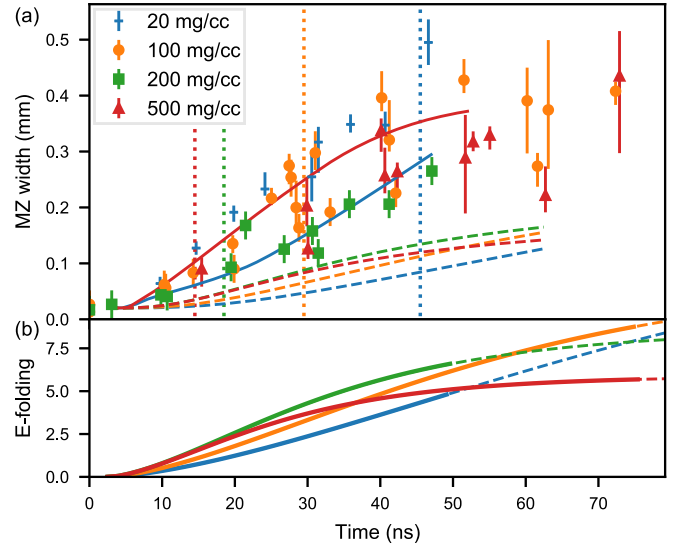

FIG. 4. (a) Evolution of the mixing zone (MZ) width as a function of time for different foam density: (20, 100, 200, and 500) mg cm^{-3} corresponding to A_t = 0.97, 0.87, 0.75, and 0.47. The vertical dotted lines indicate the time of maximum deceleration for each density at (45.5, 29.5, 18.5, and 14.5) ns, respectively. The dashed lines correspond to a modified buoyancy-drag model [50] using the experimental parameters (initial Atwood number and modulation) and the deceleration from our model. The full lines correspond to the addition of 1D expansion to the previous model [51,52]. (b) Number of e-foldings (with an extrapolation dashed) for each foam.

motion, then the phase will start (4.1, 10.6, and 21.9) ns after shock break out for the (500, 200, and 100) mg cm^{-3} foam respectively. In the case of the 20 mg cm^{-3}, the mass swept up in the foam is never equivalent to the mass of the pusher, the latter being too dense. This assumes, however, that our model stays true even at long time for this foam density.

IV. GROWTH OF THE RTI

We now consider the actual RTI growth, and measured MZ width dynamics. As clearly shown by Fig. 4(a), the growth of the MZ (which here corresponds approximately to the growth of the bubble) is faster with a high Atwood number. In Fig. 4(a) we draw with vertical dotted lines the deceleration time for each foam density as calculated previously with our model. As seen in Fig. 3(b), the deceleration attains its maximum at this time, and so should the RTI growth rate. When comparing the different RT growths, we can clearly see that the instability grows faster with the lower density foam (20 mg cm^{-3}) than with the higher one (500 mg cm^{-3}). This shows the preponderance of the effect of the foam density over the Atwood number compared to the deceleration. Two main explanations could be envisioned: either the difference in deceleration is too small to compensate for the difference in Atwood number, or nonlinear effects affect the growth of the instability.

Let us consider the first hypothesis. If we take into account only the extreme foam values, (20 and 500) mg cm^{-3}, their maximal decelerations are, respectively, (0.33 ± 0.02 and

1.15 ± 0.03) μm ns^{-1}, according to our model. Now if we consider their respective Atwood number unchanged (same compression and relaxation of the pusher and foam), then the growth rate of the higher density foam should be higher ($A_t g_{max} \sim 0.54$ μm ns^{-2} versus 0.32 for the 20 mg cm^{-3} foam). This is obviously not the case, even for early times (their deceleration cross only after ~ 35 ns). Thus the first hypothesis does not hold.

The second hypothesis is much more likely as the deformation of the interface is already well developed after a few nanoseconds, with an amplitude exceeding 0.1λ, the usual criteria for the appearance of nonlinear effects [13]. As a result of nonlinear effects, the RTI growth should become linear in time (more consistent with our late-time results), and the bubble velocity should tend to an asymptotic value [17,18] proportional to $[(\rho_1 - \rho_2)g]^{0.5}$. The difference in density is obviously lower for higher foam density, and the deceleration, which is initially higher, is quicker to tend towards zero. Since the deceleration is not sustained for high-density foam, the RTI cannot quite develop itself.

This asymptotic behavior in the RTI growth encounters a limit in the form of a reacceleration [53]. Such a phenomenon should theoretically happen when the amplitude of the instability reaches the value of its wavelength and the number of e-folding is around 8 [the e-folding is defined as the integral of the growth rate $n(t)$ as a function of time] [19,21]. As shown in Fig. 4(b), this value is not yet reached. However, those conditions should be reachable with our experimental design after 70 to 80 ns for the lighter foams (with the 500 mg cm^{-3} foam it will never be reached). This fact is also consistent with our simulations. As shown in Fig. 2(d) the vorticity, as predicted after 25 ns of evolution, is mostly concentrated around the spike's head (so at the bottom of the bubble), yet the reacceleration phenomenon is believed to be a consequence of the vorticity accumulation at the tip of the bubble. All these elements confirm that the reacceleration stage has been approached but not yet reached.

We also notice that our MZ width measurements do not match classical buoyancy-drag models as presented in [13,54,55] nor improved ones taking into account time-dependent accelerations [50,56]. In every cases taking our modeled acceleration as an input, the MZ is underestimated by a factor higher than two. Furthermore, the obtained order for the MZ growth as a function of the foam density is contrary to the experiment: a quicker growth of the 500 mg cm^{-3} compared to the 20 mg cm^{-3} is predicted. This can be seen in Fig. 4(a), where the model which bears the best results [50] is displayed in dashed line.

The MZ width evolution, however, is not solely due to RTI growth. Material expansion should also be taken into account and may represent a large fraction of the MZ [14]. In contrast, pure, non-HED RTI develops in the absence of shock waves, so there is no interaction with a shock or expansion to consider. Following the procedure described in [51,52], the background decompression contribution is evaluated by considering the velocity divergence taken from 1D FLASH4 simulations [57]. This leads to values closer to our experimental observations [see Fig. 4(a), plain lines], but it does not reorder the curves as needed. In particular, the 20 mg cm^{-3} remains underestimated. This could be due to inaccuracy in

the foam EOS for this low-density material [58]. However, our results at $A_t \simeq 1$ corroborate recent works showing that RTI spikes exhibit a strong dependence on the Atwood number in HED [27,56]. Spikes could enter in a free-fall regime for any acceleration profile at lower Atwood number than predicted by all models. The presence of a self-generated magnetic field (Biermann-battery effects) is also not taken into account in the models. Magnetic fields wrap around the RTI spikes [33], laterally confining and sharpening them, enhancing their growth. The actual bubble morphology, as observed in Fig. 1, with a thin wedgelike extremity at late time [Figs. 1(b) and 1(c)], is consistent with such interpretation. We can also note that this structure is more prominent in the lighter foam case. Investigating further low-density foams ($A_t \simeq 1$) in the deep nonlinear stage is relevant for ICF. A higher than expected RTI growth was also observed and remains unexplained in highly nonlinear ablative RTI experiments [37,38].

V. CONCLUSION

In summary, we report on a parametric study of the RTI in decelerating phase. We performed experiments on the LULI2000 high-power laser facility using a direct drive approach to put into motion the modulated rear side of a solid target. The expansion of this target into a foam, used as a deceleration medium, is RT unstable. In these HED experiments, we changed the foam density, resulting in both a variation of initial Atwood number across the interface and a variation interface deceleration. Both effects have an opposite contribution to the RTI growth, leading to a competition between them. By analogy with SNR case and by proceeding to some physical consideration, we developed an analytic model to describe the interface motion. Strikingly, this simple model reproduces our experimental data reasonably well with regard to the motion of this interface. Concerning the RTI growth, we note that the perturbation has a faster growth with a low-density foam, so in the case of high Atwood number and low deceleration. However, given the acceleration obtained by derivation of our model, the obtained growths cannot be explained using classical RTI models such as the buoyancy-drag model. We attribute this fact to the specificity of the HED physical domain. Mainly, the pressure gradient, due to the proximity of the shock and expansion of the plasma, modifies the classical RTI growth, in particular by obstructing the spike growth. We ascertain the role of this gradient, using FLASH4 simulations, and add its effect to the classical RTI growth model. The result is closer to the experiment, but still the agreement is not perfect. Other phenomena, such as the effect of the magnetic field or the reacceleration, might also play a role and should be considered in future work.

We believe that scaling this platform on a MJ scale laser facilities [53] in association with high-resolution x-ray imaging diagnostics [36] could provide an accurate tool to study the heretofore inaccessible role of vorticity in late-time RTI growth [21].

APPENDIX A: ERRORS AND UNCERTAINTIES

In this article, error bars and uncertainties appear in several place, but they do not always hold the same meaning. We should distinguish between three kind of error bars. The first one is linked to the measure of different position (spike, bubbles) on the radiographs and simulations. Figures 2(a) and 3(a) possess this kind of error bar. The second kind corresponds to the error of the value calculated from the data of the first category. This error is directly derived from the first one and can be seen as the propagation of the previous error. This mainly concerns Fig. 4(a). Finally the errors which are linked to the model and the regression make the third kind.

1. Error on the interface position

The error in the measure position on the experimental x-ray radiographs has several origins. First, the x-ray radiograph has some limitation in resolution. This is partly due to the photo-cascade inside the image plate, which broadens the zone being illuminated. Another point to consider is the geometry of the radiography system, a point projection scheme. Due to the shadow and penumbra geometrical property the resolution is limited to the size of the source, ~ 25 μm. The temporal deterioration of the resolution due to motion blurring is here negligible compared to the other phenomena as the exposure time is of the order of 10 ps for a shock velocity lower than 30 μm ns^{-1}.

To the previous effects, which are intrinsic to the radiography technique employed, we should add the possible spatial variation of the lighting. These variations are due to phenomena of self-shadowing of the back-lighter and other variations that may affect the x-ray source (interaction of a titanium wire and a picosecond laser). This leads to spatial nonuniformity is the lighting, which may be a source of error for our measure in some specific cases, where an abrupt variation coincides with the interface position.

Finally the diffusion of the plasma at the interface between pusher and foam leads to the apparition of absorption gradients. As a result, there is no sharp interface at late time.

Two approaches, which bear the same results, were employed to measure the interface position. The simplest one, described in [40], consists of finding the interface by eye. The appreciation of each image in its entirety allows surprisingly good results for this method.

The second method consists of performing a line-out on the spike and bubble axis (see Fig. 5). On this line-out the signal above the pusher (V_p) is different from the one above the foam ($V_f > V_p$). The interface corresponds to the transition between both. We should mention here that this transition is not always symmetric. In such a case, we define the position of the interface (x_i) at the midvalue [$V(x_i) = (V_p + V_f)/2$], and we measure both positive [$\sigma^+ = x_+ - x_i$, with $V(x_+) = 0.9V_f + 0.1V_p$] and negative [$\sigma^- = x_i - x_-$, with $V(x_-) = 0.1V_f + 0.9V_p$] error bars. These result in asymmetric errors. Some other methods
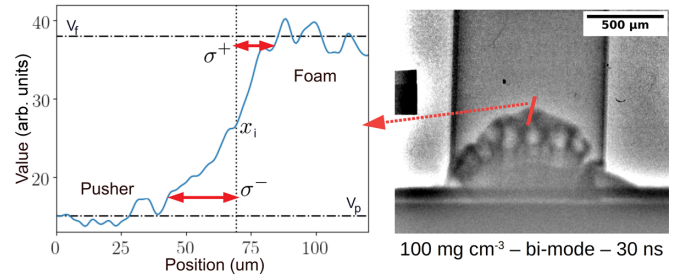

FIG. 5. Position of the spike and asymmetric error bars. A line-out is performed on a x-ray radiograph of a 100 mg cm^3 bimode target, 30 ns after laser shot. This line-out centered on the spike position shows an asymmetry on its intensity profile. This asymmetry is used to define the error bars.

exist [32,59], but they could not be employed in the present experiments.

2. Mixing zone-error composition

To obtain the mixing zone width, we subtracted the bubble position to the position of the spike. Since both possess asymmetric error, the error on the mixing zone is a composition of both error [60]. Here we define the error on the mixing zone as $\sigma_{MZ}^{\pm} = \sqrt{(\sigma_{spike}^{\pm}{}^2 + \sigma_{bubble}^{\mp}{}^2)/2}$. This formula leads to an overestimation of the error.

3. Fitting and error

The last type of error previously mentioned are the uncertainties related to the model and the value of its fitting parameters. These parameters are obtained by fitting data with asymmetrical errors. To do so we supposed that the asymmetric error bars correspond to two half-normal deviation. We randomly take a value for each data point using such a probability distribution and proceed to the fitting of the data using a least square method. We repeat this process 2000 times and obtain a distribution of possible values for each parameter. This allows us to define the value of each parameter and their asymmetric error bars. In this paper we keep only the higher value for their error, making it symmetric.

APPENDIX B: BUOYANCY-DRAG MODEL APPLICATION

One of the unexpected results of this article is the noncompliance of the experiment to the buoyancy-drag model or as shown in Fig. 4(a) to an improved version of it. This came as a surprise since these models can be used to describe the global growth of the RTI, even though they are more often used to describe late-time evolution of the instability.

1. Model and method

The model evolution displayed in Fig. 4(a) with dashed lines is a direct application of the improved buoyancy-drag model with time-dependent acceleration directly taken from [50]. In this model, the following equation is solved:

$$\ddot{\theta}_L - g(t)k_L A_L \theta_L = 0 \qquad (B1)$$

with $\theta_L \equiv e^{k_L(\eta - \eta_0)}$, $k_L \equiv (c(1+c)(1+A_t)k)/(2+2c+2cA_t-2A_t)$, $A_L \equiv 2A_t/(1+c+cA_t-A_t)$. Here η is the

TABLE I. Different physical parameters obtained from the FLASH simulations 30 ns after the laser shot. The shock foam density shows the variation of density from the shock to the place near the expanding pusher. $u.a.$ is the atomic mass unit.

Parameter	Formula	20 mg cm^{-3}	500 mg cm^{-3}
Shocked foam density (ρ, mg cm^{-3})	Simulated	0.4 to 0.6	0.8 to 8.7
Temperature ($T_e = T_i$, eV)	Simulated	5.3	4.9
Pressure (Mbar)	Simulated	0.05	0.11
Ionization (Z)	Thomas-Fermi model	1.16	1.29
Ion density (n_i, 10^{10} μm^{-3})	ρ/m_i	3.1	6.2
Electron density (n_e, 10^{10} μm^{-3})	$n_i Z$	3.6	8.0
Coulomb logarithm (ln Λ)	[61]	2.7	2.2
Ion thermal collision frequency (τ_i, 10^5 ns)	$4.8 \times 10^{-8} Z^4 n_i \ln \Lambda / [(m_i/u.a.)^{0.5} T_i^{1.5}]$	2.1	5.6
Ion thermal velocity (v_i, μm ns^{-1})	$9.79 \times 10^5 [T_i/(m_i/u.a.)]^{0.5}$	7.9	7.6
Ion collisional length (10^{-5} μm)	v_i/τ_i	3.8	1.4
Electron thermal collision frequency (τ_e, 10^7 ns^{-1})	$2.91 \times 10^{-6} n_e \ln \Lambda T_e^{-1.5}$	2.3	4.6
Electron thermal velocity (v_e, 10^2 μm ns^{-1})	$4.19 \times 10^7 T_e^{0.5}$	9.7	9.3
Electron collisional length (10^{-5} μm)	v_e/τ_e	4.2	2.0
Radiative cooling time (10^4 ns)	[62] Eq. (22)	9.9	2.5

the amplitude of the modulation, $\eta_0 = \eta(t = 0)$ is its initial value, g is the opposite of the acceleration of the interface obtained through our model ($-\ddot{x}$), k is the wave vector of the perturbation, and A_t the Atwood number. c is a parameter which depends on the dimension of the problem being equal to 2 in two dimensions and 1 in three dimensions. In Fig. 4(a), c is taken equal to 1, but there is no significant difference when using its other value. The definition of g as the opposite of the acceleration is taken in order to be consistent with the definition of [50] (positive Atwood number and an acceleration of the interface, g, defined positive when pointing toward the high-density medium).

To solve this model, a fourth-order Runge-Kutta algorithm was implemented. The initial parameters were taken to correspond to the experiment. The initial Atwood number was used as is, not taking into account the compression due to the shock and the following expansion. The same was done for the interface perturbation, which was initialized with a 10 μm amplitude and no initial velocity. On that topic, we should report the use of other initial parameters whose results are not displayed in this article. Indeed, we also tried to use for the initial amplitude and velocity the value obtained in our simulations after shock breakthrough as well as other values in between. The addition of an initial velocity allows us to reproduce the initial RTI growth up to approximately 10 ns when fine tuned. However, the model gives a result similar to those displayed in Fig. 4(a) for later time. The initial velocity just adds a slight concavity at the beginning of the curve before it transitions to its first convexity.

Classical buoyancy-drag models were also tried without more success. They were solved using a fourth-order Runge-Kutta algorithm and used the same initial parameters as reported above. The only exception is the acceleration, which should be fixed for this classical model and was thus taken to its mean value (we also tried a time-dependent one).

2. 1D expansion

As reported in the article, one of the downfalls of the previous model is its inability to take into account HED phenomena, such as the pressure gradient resulting from the presence of a shock and the expansion of the material. To take into account such an expansion, we followed the method described in [51,52,57]. This method follows several steps.

First, at least four simulations should be performed. Two are 2D simulations, one of which should reproduce the experimental results with the modulated target, and the other one uses a flat target. The simulation with a modulated target is both used to fine tune the laser energy used in simulations and to obtain a better time discretization for the temporal position of both spike and bubbles. The other simulations are 1D simulations. Since the modulation of the interface cannot be reproduce in one dimension, three values for the initial thickness of the pusher can be chosen: the spike (30 μm), the bubble (50 μm), or the interface in between (40 μm). Since the simulation code will give slightly different results in one and two dimensions, we fine tune the laser energy used in one dimension using the 2D simulation of the flat target and the 1D one with a 40 μm pusher. Finally, the 1D simulation using a 50 μm pusher is performed. The 30 μm pusher simulation can also be performed at that point, but it holds less value in our case, since the RTI growth comes mainly from the bubbles.

The second step consists of extracting the fluid velocities at the right position from the 1D simulations. By using 1D simulations the fluid velocity depends only on the expansion of the material, and it does not contained the RTI contribution, contrary to 2D simulations. The "right" position is the position of the bubbles and spikes interface taken from the 2D simulations and reported for their respective 1D simulations. In other words, we extract the fluid velocity from the 1D simulations at the position, where an element characterizing the RTI is expected to be with more dimensions. Since the time steps might not match exactly between one and two dimensions, and since the spatial resolution will also differ due to the AMR, we proceed to two consecutive cubic interpolations. The first one for the temporal evolution of the RTI elements is seen in two dimensions, so we can find its position for each time step of the corresponding 1D simulation. The second one is for the

spatial velocity variation of the 1D simulations to obtain its value at the right position.

From the previously obtained velocities, an expansion velocity is calculated. It consists of the 1D velocity difference between interface and bubble or interface and spike. By integrating this expansion velocity, time-dependent spatial expansions $E(t)$ are obtained in both the bubble and spike direction:

$$E_{\text{bubble}}(t) = \int_0^t [v_{\text{interface}}(t') - v_{\text{bubble}}(t')]dt'. \quad \text{(B2)}$$

This spatial expansion is simply added to the results of the buoyancy-drag model. Thus, the resulting RTI amplitude, $\tilde{\eta}$, is equal to $\tilde{\eta}(t) = \eta(t) + E(t)$ (reusing previous notation).

APPENDIX C: PHYSICAL PARAMETERS

Some physical parameters that characterize this experiment are displayed in Table I. They were obtained through our 2D simulations.

[1] L. Rayleigh, Investigation of the character of the equilibrium of an incompressible heavy fluid of variable density, Proc. Lond. Math. Soc. **14**, 170 (1883).

[2] G. I. Taylor, The instability of liquid surfaces when accelerated in a direction perpendicular to their planes, Proc. R. Soc. London A **201**, 192 (1950).

[3] K. Sasaki, N. Suzuki, D. Akamatsu, and H. Saito, Rayleigh-Taylor instability and mushroom-pattern formation in a two-component Bose-Einstein condensate, Phys. Rev. A **80**, 063611 (2009).

[4] R. Chevalier and R. Klein, On the Rayleigh-Taylor instability in stellar explosions, Astrophys. J. **219**, 994 (1978).

[5] J. B. Bell, M. S. Day, C. A. Rendleman, S. E. Woosley, and M. Zingale, Direct numerical simulations of type Ia supernovae flames. II. The Rayleigh-Taylor instability, Astrophys. J. **608**, 883 (2004).

[6] U. D'Ortona and N. Thomas, Self-Induced Rayleigh-Taylor Instability in Segregating Dry Granular Flows, Phys. Rev. Lett. **124**, 178001 (2020).

[7] A. Hillier, The magnetic Rayleigh-Taylor instability in solar prominences, Rev. Modern Plasma Phys. **2**, 1 (2018).

[8] W. Gorczyk, B. Hobbs, and T. Gerya, Initiation of Rayleigh-Taylor instabilities in intra-cratonic settings, Tectonophysics **514**, 146 (2012).

[9] C. P. Conrad and P. Molnar, The growth of Rayleigh-Taylor-type instabilities in the lithosphere for various rheological and density structures, Geophys. J. Int. **129**, 95 (1997).

[10] R. D. Petrasso, Rayleigh's challenge endures, Nature (London) **367**, 217 (1994).

[11] A. Casner, C. Mailliet, G. Rigon, S. Khan, D. Martinez, B. Albertazzi, T. Michel, T. Sano, Y. Sakawa, P. Tzeferacos *et al.*, From ICF to laboratory astrophysics: Ablative and classical Rayleigh–Taylor instability experiments in turbulent-like regimes, Nucl. Fusion **59**, 032002 (2018).

[12] Y. Zhou, Rayleigh-Taylor and Richtmyer-Meshkov instability induced flow, turbulence, and mixing. I, Phys. Rep. **720–722**, 1 (2017).

[13] Y. Zhou, Rayleigh-Taylor and Richtmyer-Meshkov instability induced flow, turbulence, and mixing. II, Phys. Rep. **723–725**, 1 (2017).

[14] O. Schilling, Progress on understanding Rayleigh-Taylor flow and mixing using synergy between simulation, modeling, and experiment, J. Fluids Eng. **142**, 120802 (2020).

[15] P. Ramaprabhu, G. Dimonte, Y.-N. Young, A. C. Calder, and B. Fryxell, Limits of the potential flow approach to the single-mode Rayleigh-Taylor problem, Phys. Rev. E **74**, 066308 (2006).

[16] A. Hillier, Self-similar solutions of asymmetric Rayleigh-Taylor mixing, Phys. Fluids **32**, 015103 (2020).

[17] D. Layzer, On the instability of superposed fluids in a gravitational field, Astrophys. J. **122**, 1 (1955).

[18] V. N. Goncharov, Analytical Model of Nonlinear, Single-Mode, Classical Rayleigh-Taylor Instability at Arbitrary Atwood Numbers, Phys. Rev. Lett. **88**, 134502 (2002).

[19] P. Ramaprabhu, G. Dimonte, P. Woodward, C. Fryer, G. Rockefeller, K. Muthuraman, P.-H. Lin, and J. Jayaraj, The late-time dynamics of the single-mode Rayleigh-Taylor instability, Phys. Fluids **24**, 074107 (2012).

[20] T. Wei and D. Livescu, Late-time quadratic growth in single-mode Rayleigh-Taylor instability, Phys. Rev. E **86**, 046405 (2012).

[21] X. Bian, H. Aluie, D. Zhao, H. Zhang, and D. Livescu, Revisiting the late-time growth of single-mode Rayleigh-Taylor instability and the role of vorticity, Physica D **403**, 132250 (2020).

[22] R. Betti and J. Sanz, Bubble Acceleration in the Ablative Rayleigh-Taylor Instability, Phys. Rev. Lett. **97**, 205002 (2006).

[23] D. S. Clark and M. Tabak, Nonlinear Rayleigh-Taylor growth in converging geometry, Phys. Rev. E **71**, 055302(R) (2005).

[24] L. Pickworth, B. Hammel, V. Smalyuk, H. Robey, R. Tommasini, L. Benedetti, L. Berzak Hopkins, D. Bradley, M. Dayton *et al.*, Development of new platforms for hydrodynamic instability and asymmetry measurements in deceleration phase of indirectly driven implosions on NIF, Phys. Plasmas **25**, 082705 (2018).

[25] J. P. Sauppe, S. Palaniyappan, B. J. Tobias, J. L. Kline, K. A. Flippo, O. L. Landen, D. Shvarts, S. H. Batha, P. A. Bradley, E. N. Loomis *et al.*, Demonstration of Scale-Invariant Rayleigh-Taylor Instability Growth in Laser-Driven Cylindrical Implosion Experiments, Phys. Rev. Lett. **124**, 185003 (2020).

[26] J. W. Jacobs and I. Catton, Three-dimensional Rayleigh-Taylor instability Part 2. Experiment, J. Fluid Mech. **187**, 353 (1988).

[27] R. Morgan, W. Cabot, J. Greenough, and J. W. Jacobs, Rarefaction-driven Rayleigh-Taylor instability. Part 2. Experiments and simulations in the nonlinear regime, J. Fluid Mech. **838**, 320 (2018).

[28] R. Morgan and J. Jacobs, Experiments and simulations on the turbulent, rarefaction wave driven Rayleigh-Taylor instability, J. Fluids Eng. **142**, 121101 (2020).

[29] Z. Huang, A. De Luca, T. J. Atherton, M. Bird, C. Rosenblatt, and P. Carlès, Rayleigh-Taylor Instability Experiments with

Precise and Arbitrary Control of the Initial Interface Shape, Phys. Rev. Lett. **99**, 204502 (2007).

[30] S. S. Orlov, S. I. Abarzhi, S. B. Oh, G. Barbastathis, and K. R. Sreenivasan, High-performance holographic technologies for fluid-dynamics experiments, Philos. Trans. R. Soc. London A **368**, 1705 (2010).

[31] B. A. Remington, H.-S. Park, D. T. Casey, R. M. Cavallo, D. S. Clark, C. M. Huntington, C. C. Kuranz, A. R. Miles, S. R. Nagel, K. S. Raman *et al.*, Rayleigh-Taylor instabilities in high-energy density settings on the National Ignition Facility, Proc. Natl. Acad. Sci. USA **116**, 18233 (2019).

[32] J. D. Bender, O. Schilling, K. S. Raman, R. A. Managan, B. J. Olson, S. R. Copeland, C. L. Ellison, D. J. Erskine, C. M. Huntington, B. E. Morgan *et al.*, Simulation and flow physics of a shocked and reshocked high-energy-density mixing layer, J. Fluid Mech. **915**, A84 (2021).

[33] C. C. Kuranz, R. P. Drake, M. J. Grosskopf, B. Fryxell, A. Budde, J. S. Hansen, A. R. Mile, T. Plewa, N. Heam, and J. Knauer, Spike morphology in blast-wave-driven instability experiments, Phys. Plasmas **17**, 052709 (2010).

[34] C. C. Kuranz, H.-S. Park, C. M. Huntington, A. R. Miles, B. A. Remington, T. Plewa, M. R. Trantham, H. F. Robey, D. Shvarts, A. Shimony *et al.*, How high energy fluxes may affect Rayleigh-Taylor instability growth in young supernova remnants, Nat. Commun. **9**, 1564 (2018).

[35] G. Rigon, A. Casner, B. Albertazzi, T. Michel, P. Mabey, E. Falize, J. Ballet, L. Van Box Som, S. Pikuz, Y. Sakawa *et al.*, Rayleigh-Taylor instability experiments on the LULI2000 laser in scaled conditions for young supernova remnants, Phys. Rev. E **100**, 021201(R) (2019).

[36] G. Rigon, B. Albertazzi, T. Pikuz, P. Mabey, V. Bouffetier, N. Ozaki, T. Vinci, F. Barbato, E. Falize, Y. Inubushi *et al.*, Micron-scale phenomena observed in a turbulent laser-produced plasma, Nat. Commun. **12**, 2679 (2021).

[37] D. A. Martinez, V. A. Smalyuk, J. O. Kane, A. Casner, S. Liberatore, and L. P. Masse, Evidence for a Bubble-Competition Regime in Indirectly Driven Ablative Rayleigh-Taylor Instability Experiments on the NIF, Phys. Rev. Lett. **114**, 215004 (2015).

[38] A. Casner, L. Masse, S. Liberatore, P. Loiseau, P. E. Masson-Laborde, L. Jacquet, D. Martinez, A. S. Moore, R. Seugling, S. Felker *et al.*, Probing the deep nonlinear stage of the ablative Rayleigh-Taylor instability in indirect drive experiments on the National Ignition Facility, Phys. Plasmas **22**, 056302 (2015).

[39] E. Brambrink, S. Baton, M. Koenig, R. Yurchak, N. Bidaut, B. Albertazzi, J. Cross, G. Gregori, A. Rigby, E. Falize *et al.*, Short-pulse laser-driven x-ray radiography, High Power Laser Science and Engineering **4**, e30 (2016).

[40] N. C. Swisher, C. C. Kuranz, D. Arnett, O. Hurricane, B. A. Remington, H. F. Robey, and S. I. Abarzhi, Rayleigh-taylor mixing in supernova experiments, Phys. Plasmas **22**, 102707 (2015).

[41] B. Fryxell, K. Olson, P. Ricker, F. X. Timmes, M. Zingale, D. Q. Lamb, P. MacNeice, R. Rosner, J. W. Truran, and H. Tufo, FLASH: An adaptive mesh hydrodynamics code for modeling astrophysical thermonuclear flashes, Astrophys. J. Suppl. **131**, 273 (2000).

[42] A. Dubey, A. Almgren, J. Bell, M. Berzins, S. Brandt, G. Bryan, P. Colella, D. Graves, M. Lijewski, F. Lffler *et al.*, A survey of high level frameworks in block-structured adaptive mesh refinement packages, J. Parall. Distrib. Comput. **74**, 3217 (2014).

[43] J. Macfarlane, IONMIX—A code for computing the equation of state and radiative properties of LTE and non-LTE plasmas, Comput. Phys. Commun. **56**, 259 (1989).

[44] J. MacFarlane, I. Golovkin, and P. Woodruff, HELIOS-CR—A 1-D radiation-magnetohydrodynamics code with inline atomic kinetics modeling, J. Quant. Spectrosc. Radiat. Transfer **99**, 381 (2006).

[45] S. G. Glendinning, J. Bolstad, D. Braun, M. Edwards, W. Hsing, B. Lasinski, H. Louis, A. Miles, J. Moreno, T. Peyser *et al.*, Effect of shock proximity on Richtmyer-Meshkov growth, Phys. Plasmas **10**, 1931 (2003).

[46] J. K. Truelove and C. F. McKee, Evolution of nonradiative supernova remnants, Astrophys. J. Supp. **120**, 299 (1999).

[47] X. Tang and R. A. Chevalier, Shock evolution in non-radiative supernova remnants, Mon. Not. R. Astron. Soc. **465**, 3793 (2017).

[48] J. M. Blondin and D. C. Ellison, Rayleigh-Taylor instabilities in young supernova remnants undergoing efficient particle acceleration, Astrophys. J. **560**, 244 (2001).

[49] F. Fraschetti, R. Teyssier, J. Ballet, and A. Decourchelle, Simulation of the growth of the 3D Rayleigh-Taylor instability in supernova remnants using an expanding reference frame, Astron. Astrophys. **515**, A104 (2010).

[50] K. O. Mikaelian, Nonlinear hydrodynamic interface instabilities driven by time-dependent accelerations, Phys. Rev. E **79**, 065303(R) (2009).

[51] A. R. Miles, Bubble merger model for the nonlinear Rayleigh-Taylor instability driven by a strong blast wave, Phys. Plasmas **11**, 5140 (2004).

[52] A. R. Miles, The blast-wave-driven instability as a vehicle for understanding supernova explosion structure, Astrophys. J. **696**, 498 (2009).

[53] G. Malamud, L. Elgin, T. Handy, C. Huntington, R. Drake, D. Shvarts, A. Shimony, and C. Kuranz, Design of a single-mode Rayleigh-Taylor instability experiment in the highly nonlinear regime, High Energy Density Phys. **32**, 18 (2019).

[54] G. Dimonte, Spanwise homogeneous buoyancy-drag model for Rayleigh-Taylor mixing and experimental evaluation, Phys. Plasmas **7**, 2255 (2000).

[55] D. Oron, L. Arazi, D. Kartoon, A. Rikanati, U. Alon, and D. Shvarts, Dimensionality dependence of the Rayleigh-Taylor and Richtmyer-Meshkov instability late-time scaling laws, Phys. Plasmas **8**, 2883 (2001).

[56] P. Ramaprabhu, V. Karkhanis, R. Banerjee, H. Varshochi, M. Khan, and A. G. W. Lawrie, Evolution of the single-mode Rayleigh-Taylor instability under the influence of time-dependent accelerations, Phys. Rev. E **93**, 013118 (2016).

[57] R. P. Drake, Spike penetration in blast-wave-driven instabilities, Astrophys. J. **744**, 184 (2011).

[58] K. Nagai, C. S. Musgrave, and W. Nazarov, A review of low density porous materials used in laser plasma experiments, Phys. Plasmas **25**, 030501 (2018).

[59] C. Huntington, K. Raman, S. Nagel, S. MacLaren, T. Baumann, J. Bender, S. Prisbrey, L. Simmons, P. Wang, and Y. Zhou, Split radiographic tracer technique to measure the full width of a high

energy density mixing layer, High Energy Density Phys. **35**, 100733 (2020).

[60] R. Barlow, *Asymmetric Errors*, PHYSTAT2003, SLAC, Stanford, California, 2003.

[61] T. G. White, M. T. Oliver, P. Mabey, M. Kühn-Kauffeldt, A. F. A. Bott, L. N. K. Döhl, A. R. Bell, R. Bingham, R. Clarke, J.

Foster *et al.*, Supersonic plasma turbulence in the laboratory, Nat. Commun. **10**, 1758 (2019).

[62] D. Ryutov, R. P. Drake, J. Kane, E. Liang, B. A. Remington, and W. M. Wood-Vasey, Similarity criteria for the laboratory simulation of supernova hydrodynamics, Astrophys. J. **518**, 821 (1999).